Monthly Notices
of the Royal Astronomical Society

[O III] line ratios and evolution of oxygen abundance with redshift using JWST-VLT-Keck observations

Journal:	*Monthly Notices of the Royal Astronomical Society*
Manuscript ID	Draft
Manuscript type:	Paper
Date Submitted by the Author:	n/a
Complete List of Authors:	Bhandari, Vidit; Denison University Xu, Mingyi; The Ohio State University, Astronomy Nahar, Sultana; The Ohio State University, Astronomy Pradhan, Anil; The Ohio State University, Astronomy
Keywords:	galaxies: abundances < Galaxies

MNRAS 000, 1–10 (2026) Preprint 10 February 2026 Compiled using MNRAS LATEX style file v3.3

[O III] line ratios and evolution of oxygen abundance with redshift using JWST-VLT-Keck observations

Vidit Bhandari,[1] Mingyi Xu,[2] Sultana N. Nahar,[2] Anil K. Pradhan [2,3]★
[1] *Department of Physics, Denison University, Granville, OH, USA.*
[2] *Department of Astronomy,* [3] *Chemical Physics Program, The Ohio State University, Columbus, OH, USA 43210.*

Accepted XXX. Received YYY; in original form ZZZ

ABSTRACT

Understanding chemical evolution of galaxies has been dramatically revised by JWST observations up to high redshifts $z \sim 14$, which reveal metal-rich systems forming within a few hundred million years after the Big Bang. Using new atomic data, and complemented by low-z observations from VLT and Keck, we examine a large sample of 44 galaxies to analyze or re-analyze reportedly observed [O III] line ratios up to high-z galaxies to derive electron temperatures, densities, and oxygen abundances. In addition to [O III] temperature diagnostics, [O II] and [S II] ratios are employed for density constraints and contour plots of physical conditions. Based on nebular temperature-abundance relations we may track the evolution of [12 + log(O/H)] with redshift. Our [O III] atomic model incorporates recombination-cascade contributions to forbidden lines using new level-specific recombination rate coefficients and transition probabilities, together with collision strengths computed in earlier works. We find that individual galaxies show a large and systematic variation with electron temperature in the nebular range 5000-25,000K, and O-abundance down to 6.75 compared to the solar value 8.70. The oxygen abundances vs. z display a broadly decreasing trend toward high-$z \sim 10$, with a best fit ranging from 8.25 to 7.50 from the present epoch at $z = 0$, generally consistent with previous works on metallicity-redshift variation. The present analysis employs a collisional-radiative-recombination model that also considers possible (e + O IV) –> O III recombination-cascade contributions to [O III] forbidden lines, but is found to be negligible. That implicitly implies that the analysis refers to nebular H II regions per se, and not to possibly AGN contributions that might involve higher ionization states. We also explore AI Machine Learning models to predict and complement directly derived results, with preliminary simulations trained on observed flux ratios and PyNeb-simulated datasets that are promising but limited by current sample sizes. Future work may expand datasets and refine statistical models to establish robust constraints on early-universe chemical evolution.

Key words: galaxies: abundances – galaxies: high-redshift – (ISM:) H II regions – line: formation – atomic data – atomic processes

1 INTRODUCTION

Space-based observations of distant high-z galaxies by the James Webb Space Telescope (JWST) have definitively established that galaxy formation began much earlier than believed hitherto (Stefano *et al.* 2023, Arellano-Córdova et al. 2022, Sanders et al. 2023a, Katz *et al.* , Glass-JWST Early Release Science Program. IV. Mascia *et al.* 2024). That became evident from a number of clearly resolved atomic lines from several elements other than H and He. Furthermore, since the observed spectra are in the near-IR range the observations can also be verified and complemented by ground-based observations, particularly by high-resolution spectrographs at large telescopes such as Keck and Very Large Telescope (VLT). Thus optical or even near-UV lines are observable from red-shifted objects. Since JWST spectra became available, it was noticed that several well-known lines of oxygen ions were prominent in the spectra of galaxies out to z~ 10 or greater. As oxygen is one of the most common elements, its abundance would therefore be a reliable indicator of the chemical evolution of the universe if determined accurately and from a sufficient number of galaxies. In particular, the forbidden [O III] emission lines prominently stands out in many of these JWST observations and have been used to study local physical conditions and correlations among supernovae (SNe) rates, stellar formation, galactic outflows, and galaxy masses. For example, a mass-metallicity relation has been inferred, and which shows metallicity ranges significantly smaller than the present Milky Way or solar values. Also, large equivalent width of [O III] lines have been observed, implying intense radiation fields from massive stars and blue-shifted lines from SNe and galactic outflows. (e.g. Duan *et al.* 2024, Eisenstein *et al.* 2025, Clarke *et al.* 2024). Another recent study of JWST/NIRSpec spectra examining the mass-matellacity-redshift correlations finds a significant but not large deviations from a trend towards lower metallicities with increasing redshfits (Sarkar *et al.* 2025).

In our sample we consider the earliest one at $z \sim 10$ (Abdurro'uf et al. 2024, Hsiao et al. 2025, Hsiao et al. 2024), and the latest at $z \sim 1$, observed with JWST (Welch et al. 2024).

★ Corresponding Author: pradhan.1@osu.edu

Doubly-ionized oxygen O III is well-known in observations from nebular and AGN H II regions. The forbidden [O III] lines have been studied extensively and are used widely as temperature diagnostics in H II regions in the range 1000-20,000 K. In addition, forbidden [O II] and [S II] lines are employed as electron density diagnostics (Osterbrock and Ferland 2006, Dopita and Sunterland 2003, Pradhan and Nahar 2011). Together, these ions provide temperature-density information which, in turn, can be parametrized to derive oxygen abundance since only a few ionization states are involved. Useful expressions dependent on temperature and density have been utilized to obtain abundances in H II regions (e.g. Izotov *et al.* 2006, Mendez-Delgado *et al.* 2023), expressed as 12 + log(O/H) for O relative to H. A recent work has applied strong line calibration on deriving 12 + log(O/H) vz. z relation out to z$\sim$ 3.3 using data from earlier instruments such as Keck for certain masses of galaxies (Jain et al. 2025). The JWST data with considering the theoretical atomic models is more accurate to consider high redshift galaxies out to z $\sim$ 10.

The primary requirement in order to employ theoretical models to analyze observations is accurate atomic data for relevant physical processes. In the case of forbidden lines, which usually arise from transitions among low-lying energy levels of the same electronic configuration and parity, those data primarily entail electron impact excitation and radiative transition probabilities. The dominant transitions are among levels of the ground configuration of the same parity via magnetic dipole (M1) and electric quadruple (E2) transitions. High-precision atomic data have been computed for all ions under study in the present work: O II , O III and S II (references in Pradhan and Nahar 2011, and in this work). We employ these data in a spectral modeling code SPECTRA that constructs a radiative-collisional atomic model with a 5-level energy structure to obtain line emissivities and ratios. A new extension of SPECTRA is to extend the atomic model to include level-specific (e + ion) recombination coefficients from accurate R-matrix calculations from the database NORAD (Nahar 2020, 2024; Hoy *et al.* 2023). The extended collisional-radiative-recombination (CRR) model incorporates (e + ion) recombination to a number of excited levels, and radiative decays therefrom, into the upper levels that give rise to the observed forbidden lines.

2 OBSERVATIONAL DATA ANALYSIS

Spectral data for 30 galaxies observed with JWST/NIRSpec, ground-based observations of 5 galaxies from Keck/KCWI/NIRSPEC/MOSFIRE, 7 galaxies from VLT/Shooter, 1 galaxy from CLASSY, and 1 galaxy from MOSDEF was analyzed (see References). In addition, data from a few other ground-based instruments was also obtained from literature. Detailed information on data sources is given in Appendices Table A1 and Table A2, along with reported quantitative fluxes for [O III], [O II] and [S II] lines, as well as Hβ fluxes.

The JWST line data in our collection are all from $z > 1$. For analyzing some galaxies for approximate comparison in the low-z region, we added a few galaxies from ground-based observations. The data used for lower redshift ground-based observations does not include all ground-based observations until the present epoch but a representative sample of a few points. For the galaxies that appears twice in the tables, they are analyzed using different sets of line fluxes data, as shown in Table A1. The results are arranged in the same order when reproduced in Table A3.

We collected the data for galaxies whose observed fluxes have been reported for determining spectral properties, namely unblended [O II] λ 3729, λ 3726 or unblended [S II] λ 6717, λ 6732 fine structure doublet formed by atomic structure and transitions $^4S^o - ^2 D^o_{3/3,5/3}$ that are standard density diagnostics. The temperature diagnostic [O III] λ 4363, λ 5007 lines due to the atomic transitions $^1D_2 - ^1 S_0$ and $^3P^o_2 - ^1 D_2$ respectively, that have been identified and extracted until recently available observations.

There are several cases where there are some lines missing from papers in literature. However, our line ratios analysis attempts to estimate their intensities from theoretical line emissivity calculations described below. In particular, if [O III] λ 4959 is missing (necessary for the Oxygen abundance formula from Izotov et al. (2006)), we calculate its intensity since the ratio [O III] λ 5007/ λ 4959 = 2.88 is constant. That is because both transitions originate from the same upper level and the intensity ratio is determined by their respective A-values **?**, and independent of environment temperature or density. In cases where [O II] λ 3729,λ 3726 lines are missing then we employ the [O II] λ 7320, λ 7332 lines due to forbidden transitions $2s^2p^3(^2D^o_{3/2} - ^2 P^o_{1/2,3/2})$ (c.f. Izotov *et al.* 2006).

3 THEORY & COMPUTATIONAL METHOD AND ATOMIC DATA

The calculations described in this paper employ high-accuracy atomic data computed using the powerful R-matrix method and subsidiary codes described in this section. The CRR model includes atomic parameters discussed in the following subsections.

3.1 Energy Levels & Einstein A Coefficients

The energy level data for O III is computed using the R-matrix method (Nahar 1998) but substituted using observed energies where available from the National Institute of Standards and Technology (NIST) Atomic Spectra Database (www.nist.gov). The transition probabilities and A-coefficients are also obtained from previous R-matrix calculations and archived in the database Nahar-OSU-Radiative-Atomic-Database (NORAD; http://norad.astronomy.osu.edu).

Fig. 1 shows the atomic model of O III including the 10 well-know forbidden transitions among the 5 even-parity levels of the ground configuration $1s^22s^22p^2$: $^3P_{0,1,2}$,^{1} D_2,^{1} S_0. These levels are considered for collisional excitation. In addition, and for including (e + ion) recombiation into higher levels and radiative cascades therefrom, excited electronic configurations up to n = 10 are included.

3.2 Electron Impact Excitation

We consider collision strengths and Maxwellian averaged rate coefficients for the forbidden [O III] ground configuration transitions as in earlier works (Palay et al. 2012, Storey & Sochi 2015). The two sets of data agree within a few per cent throughout most of the temperature range of interest in nebulae, but differ somewhat at low electron temperatures $T_e < 1000K$ where the latter are to be preferred. That is because Storey & Sochi 2015 include additional correlation in the wavefunction expansion for the [O III] levels that include the excited configuration $1s^22p^6$ that correlates with the quasi-degenerate $^1S_0$ level of the ground configuration $1s^22s^22p^4$. That additional correlation gives rise to somewhat lower resonance structures near the excitation thresholds up to the $^1S_0$ level, resulting Maxwellian averaged collilsion strengths that differ from Palay et al. 2012. However, as we show later, the line emissivity ratios in the range of interest herein is hardly affected in using the two sets.

3.3 Electron-ion recombination

In order to discern possible effects due to (e + ion) recombination, i.e. $(e + O\ iv) \rightarrow O\ iii$, we considerably expand the set of excited energy levels of O III . That enables recombination into excited levels followed by radiative cascades to the 5 levels that give rise to the observed forbidden lines via dipole allowed transitions down to upper levels. The CRR code uses the extensive datasets for level-specific (e + ion) recombination and A-values from the database NORAD **?**needed to construct the radiative-cascade matrices. Contributions to upper level populations from (e + ion) recombination is then computed by SPECTRA code for particular [O II], [S II] and [O III] lines.

3.4 Line Emissivities & Ratios

The CRR model is incorporated in a code SPECTRA that computes line emissivities and diagnostic ratios from the data described above. There are two versions of SPECTRA in Fortran and C++ that have been compared against each other (Hoy *et al.* 2023).

The procedure adopted relies on the canonical [O III] λ 5007/ λ 4363 line ratio that is known to be dependent on electron temperature, and the [O II] λ 3729/ λ 3726 and [S II] λ 6717/ λ 6731 line ratios that are sensitive to electron density. However, as we note below, there are two sets of [O III] theoretical collision strengths available in literature: Palay *et al.* (2012) and Storey and Sochi (2015). We compute and compare the two sets in Fig. 1a, and find little difference in the nebular temperature range under consideration (see section Electron Impact Excitation below). Using the later Storey and Sochi (2015) data, and [O II] and [S II] collision strengths, we construct a contour plot of the full electron temperature-density range shown in Fig. 1b.

4 RESULTS

Once the temperature and density are determined from line emissivities and observed line intensity ratios we may derive the oxygen abundance. For oxygen abundance calculations, we adopt two different empirical formulae by Izotov et al. (2006) and Méndez-Delgado et al. (2023) respectively.

4.1 Formula by Izotov et al. (2006)

Izotov *et al.* (2006) re-evaluated empirical expressions for abundance determination from spectral data from emission line galaxies using the Sloan Digital Sky Survey (SDSS) for several elements. The inputs for this formula are relative line fluxes to Hβ, N_e, and T_e. Firstly, it defines $t = 10^{-4}T_e$([O III]) and $x = 10^{-4}N_e t^{-0.5}$. The following formulae are used in this work:

$$12 + \log(O^+/H^+) = \log(\frac{OII3727}{H\beta}) + 5.961 + \frac{1.676}{t} - 0.40\log(t) - 0.034t + log(1 + 1.35x) \quad (1)$$

$$12 + \log(O^+/H^+) = \log(\frac{OII7320 + OII7330}{H\beta}) + 6.901 + \frac{2.487}{t} - 0.483\log(t) - 0.013t + log(1 - 3.48x) \quad (2)$$

$$12 + \log(O^{2+}/H^+) = \log(\frac{OIII4959 + OIII5007}{H\beta}) + 6.200 + \frac{1.251}{t} - 0.55\log(t) - 0.014t \quad (3)$$

OII3727 represents the total(blended) relative flux of [OII] λ 3726 and [OII] λ 3729 to Hβ. If OII3727 is available, we could use (1) to calculate the OII abundance. If OII3727 is not available, we could use [OII] λ 7320 and [OII] λ 7330 relative fluxes by (2) to calculate the OII abundance. Also, using (3) with [OIII] λ 4959 relative flux, [OIII] λ 5007 relative flux, and electron temperature, we can calculate OIII abundance. Once we have the abundance for singly ionized state(OII) and doubly ionized state(OIII), we can add them up as (4) to get the total oxygen abundance.

$$\frac{O}{H} = \frac{O^+}{H^+} + \frac{O^{2+}}{H^+} \quad (4)$$

For a specific galaxy PJ308-21, the original paper Decarli et al. (2024) gives neither [O II] λ 3729+λ 3726 nor [O II] λ 7320+λ 7330 fluxes for using Izotov et al. (2006) oxygen abundance formula (1) or (2) to calculate $12 + \log(O^+/H^+)$. We then assume three different values for [O II] λ 3729+λ 3726 relative flux to Hβ: 0.5, 1.0, and 2.0. This assumption is based on the fact that most of other galaxies we examined have [O II] λ 3729+λ 3726 relative flux to Hβ around the range 0.5 to 2.0. Only the abundance formulae (1) from Izotov et al. (2006) are used with this assumed [O II] λ 3729+λ 3726 relative flux for PJ308-21, and density determination was done by using [S II] lines. We find that results under such assumption are quite similar, $12 + \log(O/H) = 7.99$,8.02 and 8.07 respectively. The another result for PJ308-21, by using another oxygen abundance formula from Méndez-Delgado et al. (2023)(will be discussed in 4.3), is $12 + \log(O/H) = 7.95$, which is quite similar to the results by assuming [O II] λ 3729+λ 3726 flux relative to Hβ with using Izotov et al. (2006) oxygen abundance formula (1). The first result $12 + \log(O/H) = 7.99$ is then adopted in the abundance over temperature, redshift, and lookback time plots.

4.2 Formula by Méndez-Delgado et al. (2023)

Whereas Izotov et al. 2006 express the overall oxygen abundance in terms of temperature and density dependence of O II and O III (Eq. 1-3), Méndez-Delgado et al. 2023 have presented empirical relations for the estimation of temperature and metallicity tacking account of temperature inhomogeneities in H II regions. They estimate temperature fluctuations via a factor t^2 as the deviation from a mean temperature T_0, and derive the following expression for the oxygen abundance

$$12 + \log(O/H) = (-1.07 \pm 0.09) \times 10^{-4} T_0(H^+) + (9.44 \pm 0.08), \quad (5)$$

where T_0 is the average temperature of ionized gas, which we take to be $\approx T_e$ (O III) following Méndez-Delgado et al. 2023. This is justified even if $t^2 > 0$ when one considers temperatures obtained from recombination lines as T_e([N ii] λ5755/λ6584) $\approx T_0$ (O II). That is because in the regions of low ionization the emission of H I recombination is essentially from the volume of O II where temperature inhomogeneities are negligible, or $t^2 \approx 0$.

4.3 Oxygen Abundance vs. Redshift and Lookback Time

Figs. 3 presents the results for O-abundance for all galaxies studied herein using both the Izotov et al. 2006 and Méndez-Delgado et al.

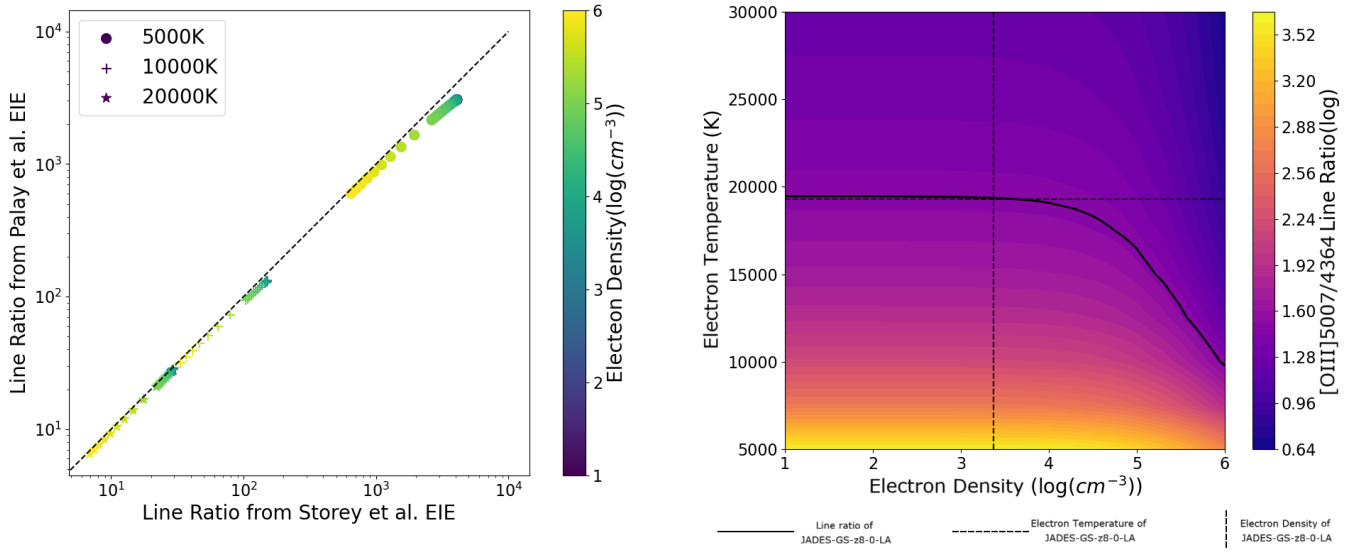

Figure 1. (Left a)Comparison between the [OIII] λ 5007/ λ 4363 line ratio results of SPECTRA code by inputting Storey & Sochi (2015) and Palay et al. (2012) effective collisional strength data. (Right b)[OIII] λ 5007/ λ 4363 line ratio contours results of SPECTRA code by inputting Storey & Sochi (2015) effective collisional strength data.

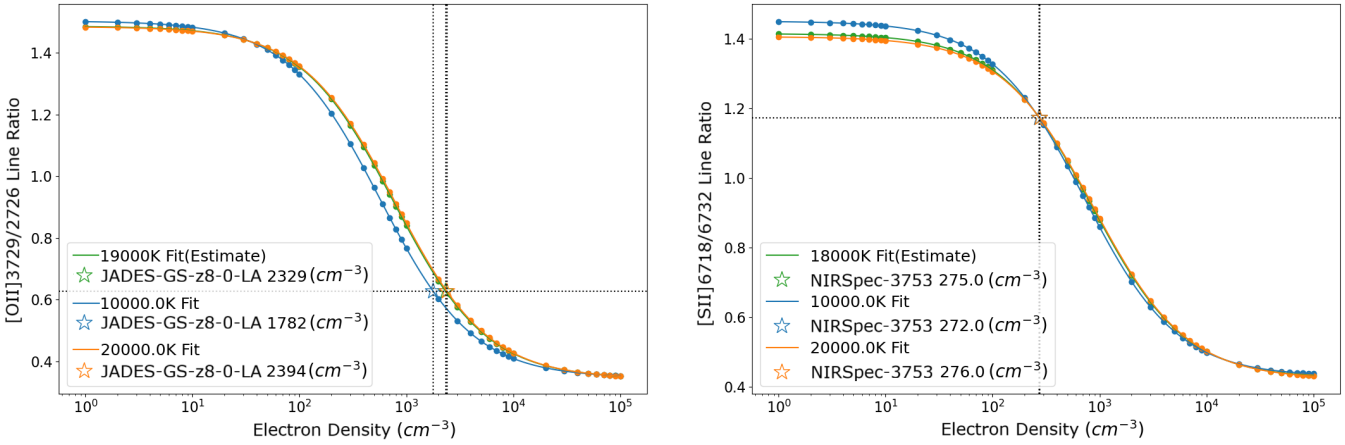

Figure 2. (Left a)[OII] λ 3729/ λ 3726 Density Diagnotics. (Right b)[SII] λ 6718/ λ 6732 Density Diagnotics.

2023 empirical formulae given above, plotted against electron temperature and color coded according to redshift z. Fig. 4 shows the results of O/H vs. z and lookback time in Gyrs, with temperature shown in the color coded bar. The lookback time was calculated from redshifts by Astropy Planck18 instance of FlatΛCDM cosmology. The results in Fig. 4 also show redshift ranges $0 < z < 1$ (blue), $1 < z < 3$ (purple), $3 < z < 6$ and $6 < z < 11$, superimposed on a linear best fit through the data.

4.4 Machine Learning Analysis

To complement the direct abundance derivations, we employ machine learning techniques to identify patterns in the parameter space and quantify predictive relationships. Our analysis uses 45 galaxies with complete measurements of z, T_e[O III], and 12 + log(O/H).

4.4.1 K-Means Clustering

Employing the elbow method, we identify $k = 3$ as the optimal cluster number. The three clusters exhibit distinct physical characteristics (Fig. 8):

- **Cluster 0** (Local/Intermediate, $n = 17$): $\langle z \rangle = 1.39 \pm 1.58$, $\langle T_e \rangle = 10{,}953 \pm 1{,}120$ K, $\langle 12+\log(O/H) \rangle = 8.29 \pm 0.15$
- **Cluster 1** (Early Universe, $n = 10$): $\langle z \rangle = 6.18 \pm 2.65$, $\langle T_e \rangle = 17{,}960 \pm 1{,}336$ K, $\langle 12+\log(O/H) \rangle = 7.68 \pm 0.15$
- **Cluster 2** (High-Redshift, $n = 18$): $\langle z \rangle = 4.73 \pm 2.26$, $\langle T_e \rangle = 14{,}439 \pm 1{,}989$ K, $\langle 12+\log(O/H) \rangle = 8.02 \pm 0.13$

Analysis of variance confirms these clusters are statistically distinct ($F = 57.43$, $p < 0.001$), with post-hoc pairwise comparisons showing significant differences between all pairs ($p < 0.001$ after Bonferroni correction). The clustering naturally separates galaxies by cosmic epoch, with clear trends in both temperature and metallicity.

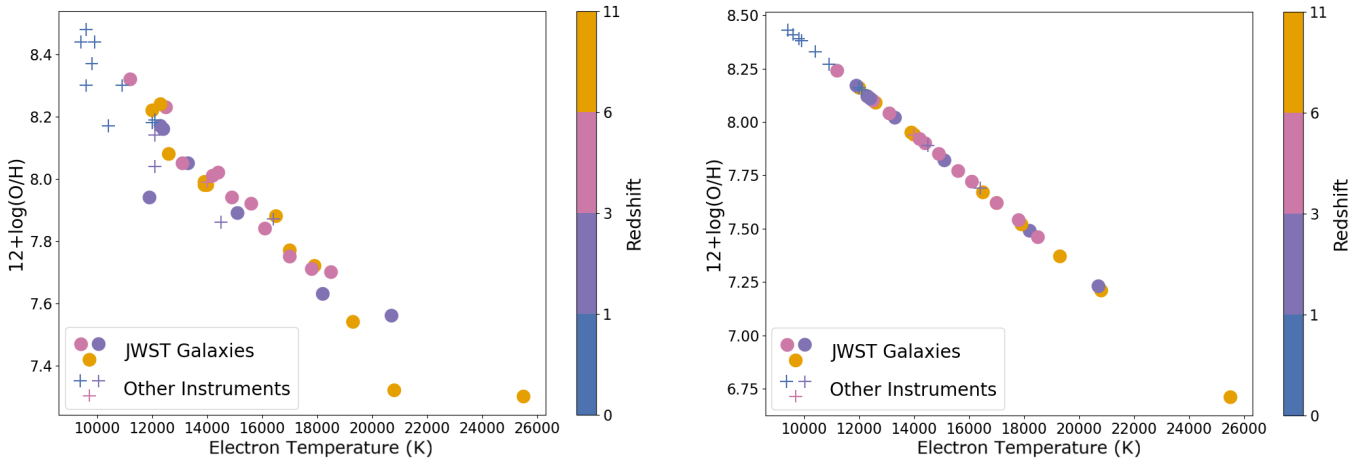

Figure 3. Oxygen Abundance Evolution with temperature using Izotov et al. (2006) formula (Left a) and Méndez-Delgado et al. (2023) formula (Right b)

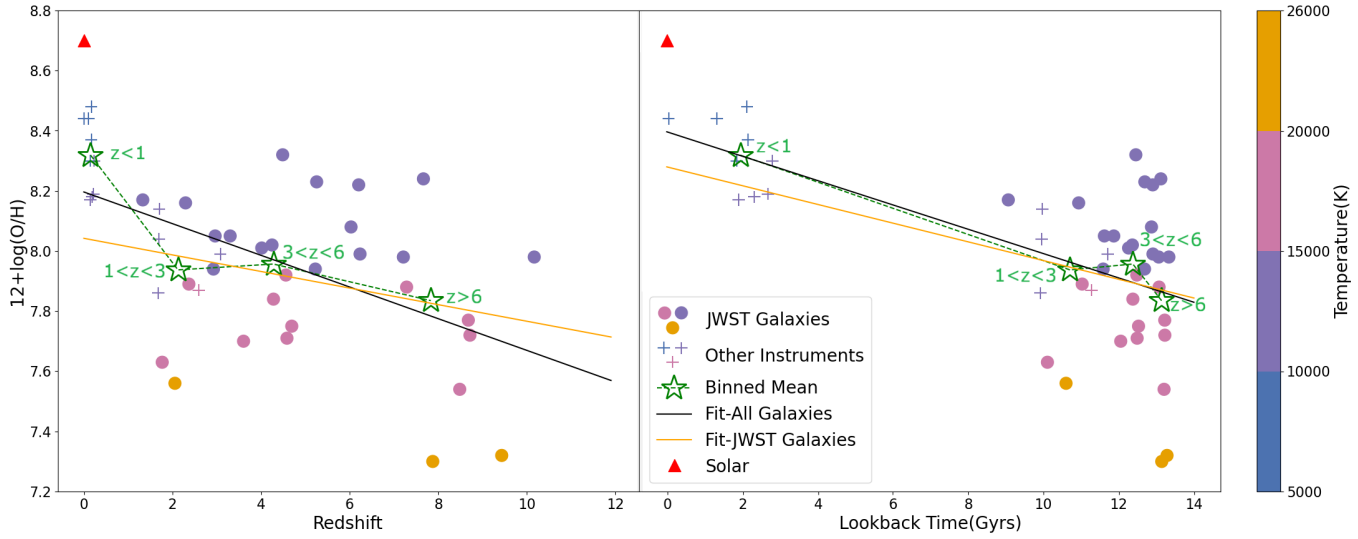

Figure 4. Oxygen abundance evolution with redshift (Left a) and lookback time (Right b) using Izotov et al. (2006) formula

4.4.2 *Predictive Regression Models*

We evaluate four regression algorithms: Linear Regression, Ridge Regression ($\alpha = 1.0$), Random Forest, and Gradient Boosting, using z and T_e as predictors. Performance is assessed via 70-30 train-test split with 5-fold cross-validation.

Ridge Regression achieves optimal performance with $R^2 = 0.832$ (test set), RMSE = 0.128 dex, and MAE = 0.089 dex (Table 1). This substantially outperforms theoretical models fit to the same data: exponential ($R^2 = 0.311$) and power law ($R^2 = 0.324$), representing a ∼160% improvement. The ensemble methods (Random Forest: $R^2 = 0.642$; Gradient Boosting: $R^2 = 0.328$) underperform likely due to the limited sample size.

The Ridge model predictions with 95% bootstrap confidence intervals (1000 iterations) are shown in Fig. 9. Residual analysis reveals no systematic trends with redshift (slope: -0.003 ± 0.008), confirming the model captures the functional form adequately. The 95% prediction interval of ±0.246 dex is comparable to typical measurement uncertainties.

Table 1. Regression model performance metrics.

Model	R^2 (test)	RMSE (dex)	MAE (dex)	R^2 (CV)
Linear Regression	0.832	0.128	0.089	0.34 ± 0.86
Ridge Regression	**0.832**	**0.128**	**0.089**	0.34 ± 0.86
Random Forest	0.642	0.186	0.110	0.18 ± 0.70
Gradient Boosting	0.328	0.255	0.131	-0.55 ± 1.42

4.4.3 *Redshift-Binned Evolution*

We partition the sample into four redshift bins and calculate weighted means (Table 2). The systematic decrease of $\Delta[12 + \log(O/H)] = 0.44$ dex from $z \sim 8$ to present corresponds to a factor of ∼2.8 increase in absolute oxygen abundance. Linear regression on binned means yields a slope of -0.052 ± 0.012 dex per unit z ($p < 0.001$), though the best-fit is better described by non-linear evolution approaching solar values asymptotically at $z \to 0$.

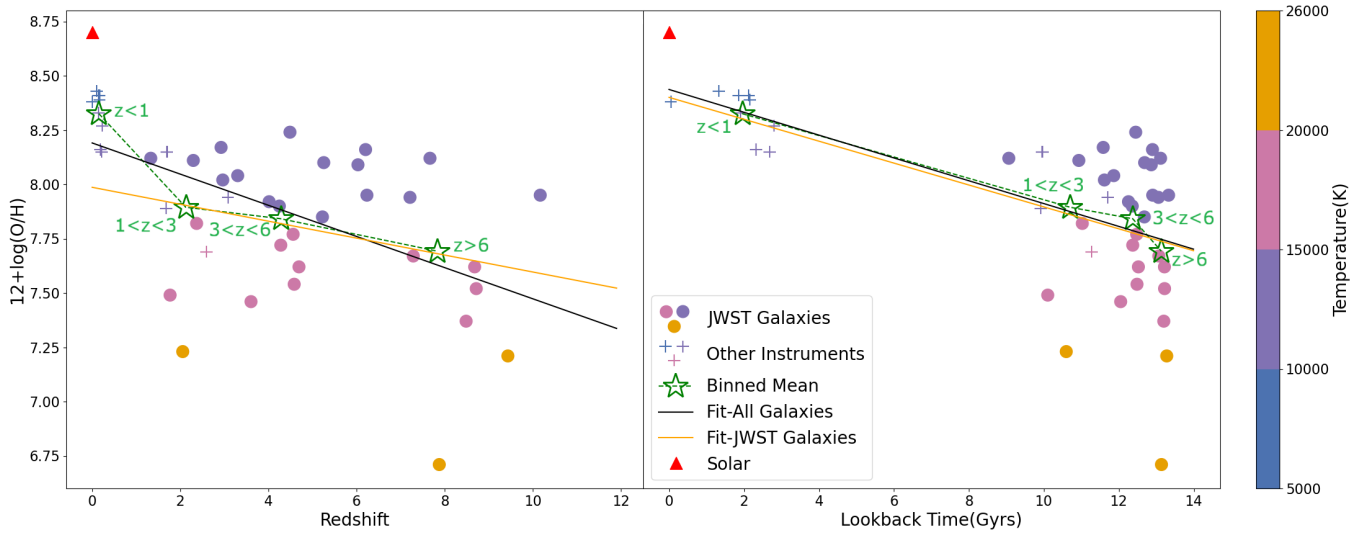

Figure 5. Oxygen abundance evolution with redshift (Left a) and lookback time (Right b) using Méndez-Delgado et al. (2023) formula

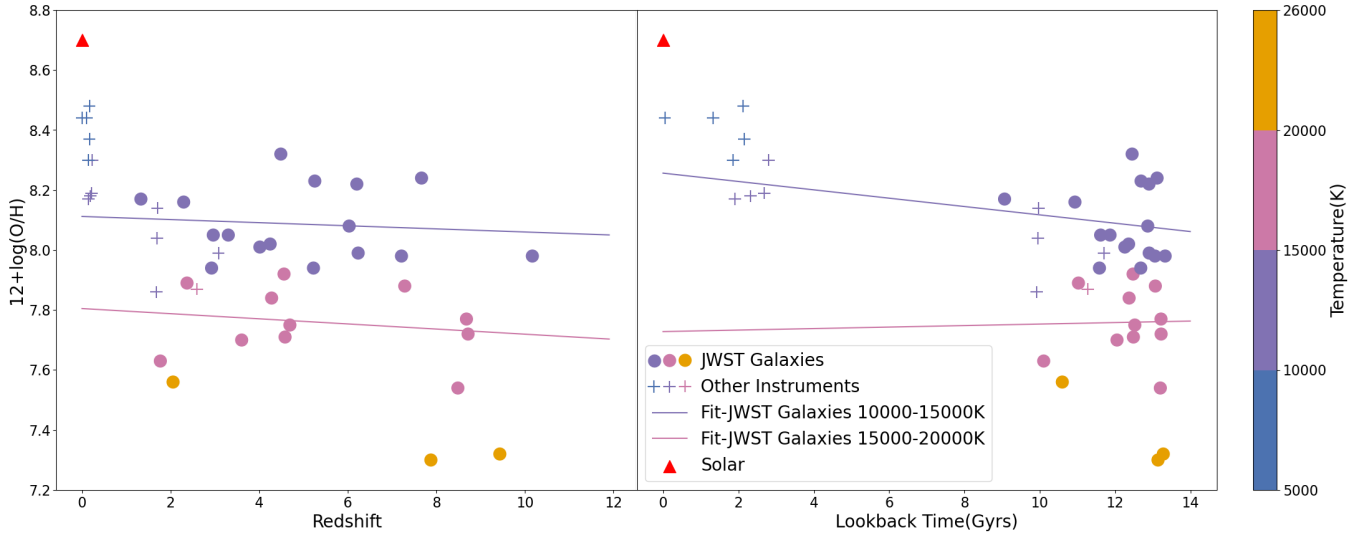

Figure 6. Oxygen abundance evolution with redshift (Left a) and lookback time (Right b) using Izotov et al. (2006) formula, with fitting to 10000-15000K and 15000-20000K temperature bins seperately

Table 2. Redshift-binned oxygen abundance statistics.

Bin	n	$\langle z \rangle$	12+log(O/H)	$\langle T_e \rangle$ (K)
$z < 1$	9	0.15 ± 0.07	8.32 ± 0.12	$10{,}411 \pm 1{,}036$
$1 \leq z < 3$	11	2.13 ± 0.55	8.06 ± 0.26	$14{,}245 \pm 3{,}188$
$3 \leq z < 6$	14	4.25 ± 0.69	7.98 ± 0.22	$14{,}593 \pm 2{,}446$
$z \geq 6$	11	7.84 ± 1.36	7.88 ± 0.28	$15{,}545 \pm 2{,}929$

4.4.4 *Physical Interpretation*

The superior performance of the bi-variate Ridge model demonstrates that chemical evolution cannot be captured by redshift alone. The strong temperature-abundance anti-correlation ($r = -0.878$, $p < 0.001$) explains much of the scatter in z-abundance space, reflecting diverse ionization conditions and star formation histories among galaxies at fixed epochs. The systematic enrichment from $z \sim 10$ to present is consistent with hierarchical galaxy formation where progressive stellar nucleosynthesis enriches the ISM over cosmic time.

The ML approach validates our direct theoretical analysis while providing statistical quantification of uncertainties. The demonstrated predictive capability ($R^2 = 0.832$) suggests this methodology can enable rapid abundance estimation for large samples where full photoionization modeling is computationally prohibitive, valuable for upcoming wide-field surveys.

5 DISCUSSION

With the aim of ascertaining a systematic pattern in metallicity with oxygen abundance as a probe, we have analyzed JWST spectra of

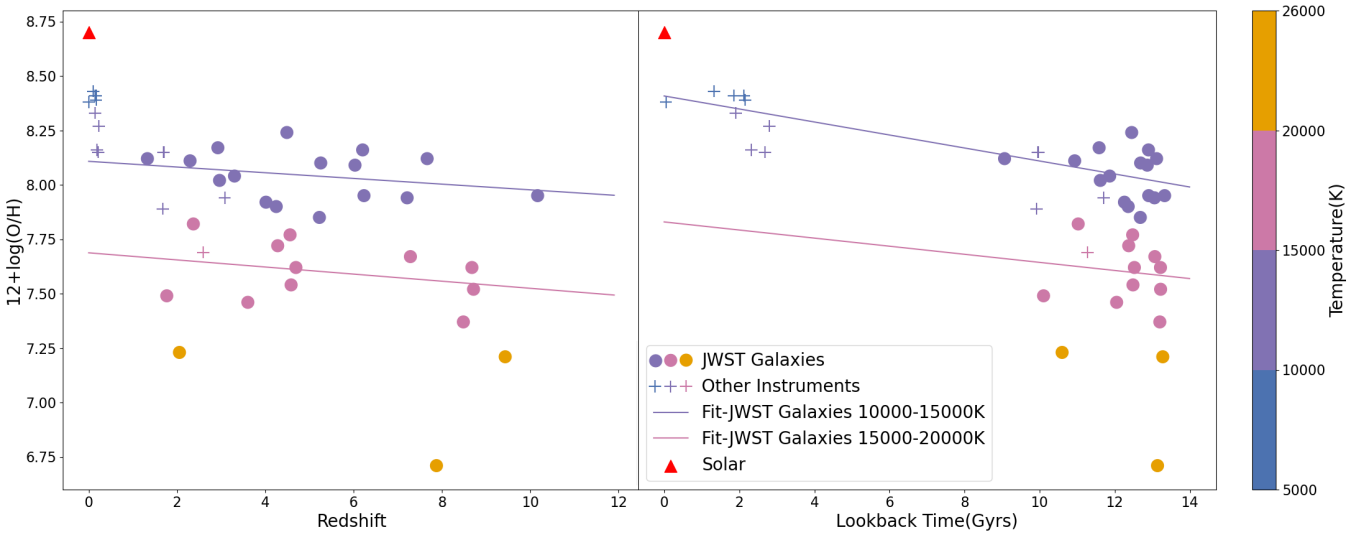

Figure 7. Oxygen abundance evolution with redshift (Left a) and lookback time (Right b) using Méndez-Delgado et al. (2023) formula, with fitting to 10000-15000K and 15000-20000K temperature bins seperately

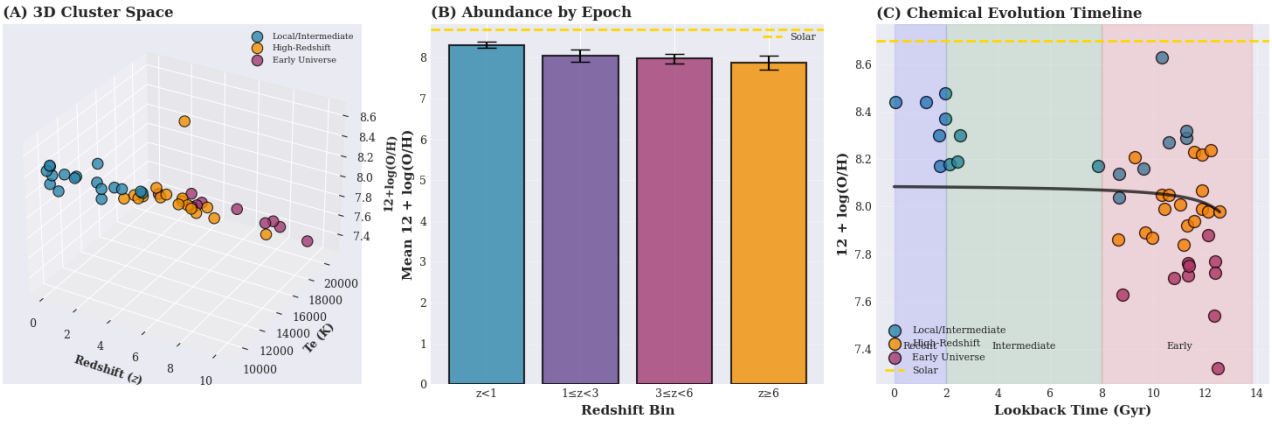

Figure 8. K-Means clustering results. *Left:* 3D parameter space showing three distinct clusters corresponding to cosmic epochs. *Center:* Mean oxygen abundance by redshift bin with 95% confidence intervals, demonstrating systematic evolution. *Right:* Chemical evolution timeline with lookback time, showing approach to solar abundance (gold dashed line) at low redshift. Shaded regions indicate cosmic epochs: Recent (blue), Intermediate (green), and Early (red) Universe.

galaxies spanning a range of redshifts from z =0-10, with the following findings and several important caveats, constraints and conundrums of the present study.

1. Broadly speaking, the results presented in the previous section demonstrate a decreasing trend in O/H with redshift as shown in Fig. 4 and 5. In each z-range selected for binning the large sample of galaxies the downward trend is discernible overall. The decreasing pattern holds according to the best linear fits as well as averages in each z-binned range.

2. Focusing on JWST galaxies in Fig. 4 and 5, which representing oxygen evolution from z=1.3293 to z=10.167, the linear best-fit between oxygen abundance and redshift gives a slope of −0.0276 and −0.0390, with y-intercept of 8.04 and 7.99 respectively. The slopes are relatively shallow, suggesting a slow evolution of metallicity in high redshift galaxies. An earlier work Sarkar et al. 2024 employed a strong linear calibration method for data analysis mainly from JADES public Data Release 3 and JWST-PRIMAL Legacy Survey ranging from z = 4-10, also suggested a slow evolution with a slope of -0.067 ± 0.013, which differs from but is close to the slope in our work. That implies that our direct T_e-based method of [O III] line ratios analysis with independent atomic processes modeling basically agrees with the strong line results in the general evolution trend of oxygen abundance with z. The data sets of our work do not entirely overlap with Sarkar et al. 2024, and therefore this agreement lends more credibility to the overall trend. While a larger sample may still be useful, these two studies appear to confirm the slow evolution of oxygen as a metallicity probe up to the early universe.

3. Whereas the lowest O-abundance is found to be 6.75 relative to solar value 8.70, the overall fits exhibit a significantly larger abundance distribution ranging from 7.50 to 8.25. That is consistently less than solar but still quite considerable, implying rapid stellar nucleosynthesis in the early Universe well beyond a lookback time of 13 Gyrs (Fig. 4 and 5).

4. There is a marked difference in O-abundance relative to electron temperature. In fact, Fig. 4 exhibits a clear dichotomy between higher temperature JWST galaxies with $T_e > 15,000K$ and signif-

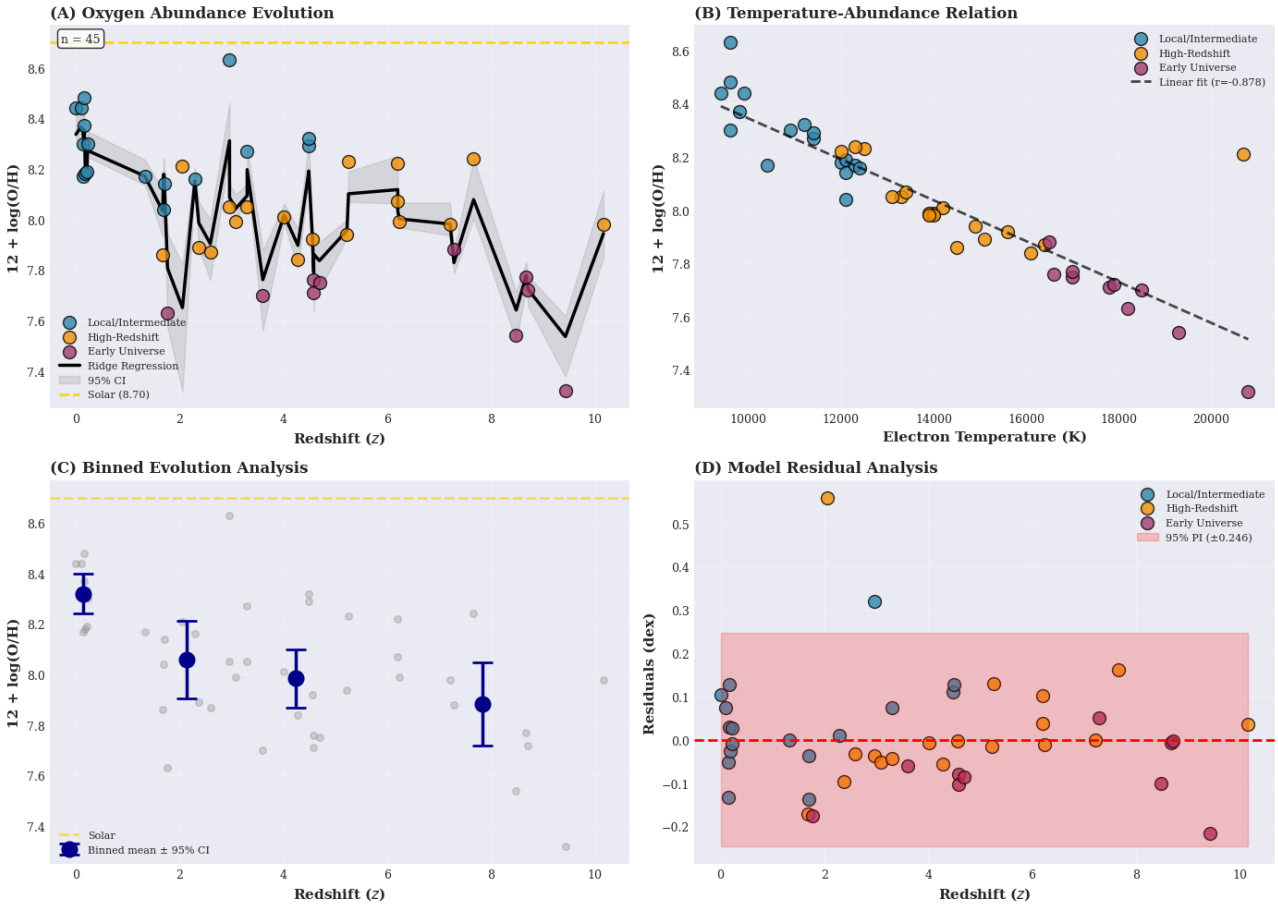

Figure 9. Machine learning regression analysis. *(A)* Oxygen abundance evolution with redshift, colored by cluster membership. Ridge regression prediction (black line) with 95% bootstrap confidence interval (gray shading). Solar abundance shown as gold dashed line. *(B)* Temperature-abundance relation demonstrating strong anti-correlation ($r = -0.878$, $p < 0.001$). *(C)* Binned evolution with error bars showing systematic enrichment (individual galaxies in gray). *(D)* Model residual analysis showing no systematic trends and 95% prediction interval (red shading, ±0.246 dex).

icantly lower oxygen abundances (pink and yellow dots), compared to those with lower temperatures with $T_e < 15,000K$ (purple dots). The scatter around the lines of best linear fit may be a measure of uncertainty in the determination of temperatures. Nonetheless, the bi-modal distribution in O-abundance with temperature seems manifest from the results derived, as shown explicitly in Fig. 6 and 7, with differential O-abundances up to ∼ 0.3 dex for the two distributions. The three galaxies with $T_e > 20,000K$ (yellow dots) most clearly elicit the inverse correlation of low O-abundance with temperature down to 12 + log(O/H) = 6.75 (Figs. 6,7).

5.The spectral diagnostics is based on nebular lines of [O II], [O III] and [S II] used to determine temperatures and densities in H II regions. Assuming that the brightest H II regions observed from high-z galaxies are due to massive stars with the shortest stellar lifespan, the spectral analysis would sample the earliest stellar formation in host galaxies. As such, the O-abundances thereby determined should correspond to metals formed close to the epochs of the earliest Type II supernovae, that are the predominant sources of α-element nucleosynthesis.

6. Additional uncertainties in nebular spectral analysis may occur owing to temperature fluctuations and (e + ion) recombinations from higher ionization stages than O III . That is a topic that requires a much larger atomic model for O III than considered herein.

7. [O III] emitters at high- z may be host galaxies with AGN. An important caveat here is the role of AGN contributions. The line ratio analysis presented herein does not distinguish between broad line regions of AGN in nebular conditions, other H II regions ionized by massive stars and supernova remnants in nebular phase. As such, further work is needed to address interesting questions related to formation of supermassive black holes in the early universe, clustering of galaxies and quasars (Huang *et al.* 2026), and objects such as Little Red Dots that may be heavily obscured AGN with similar spectral signatures (Kokorev *et al.* 2025).

8. We have ensured that the atomic data are consistent and accurate for the 5-level EIE model as well as the extended CRR model. Two different EIE datasets have been employed (Storey and Sochi 2012 and Palay *et al.* 2012), and both yield results for [O III] line ratios in the temperature range of interest, 5000-20,000 K, that are in excellent agreement for a wide range of nebular densities (Fig. 1). Combined with the O II and S II atomic data for density diagnostics they yield the colored contour temperature-density plots shown in Fig. 2. The much larger CRR model than EIE employs accurate R-matrix data for level-specific (e + ion) recombination rate coefficients from NORAD (Nahar 2020, 2024). Altogether, the atomic data lend confidence to the accuracy of computed line ratios. Therefore, the temperature-abundance dichotomy manifest in results shown as bi-modal distribution in Fig. 6

9. Results from ground based data from Keck and VLT instruments

up to $z \sim 3$ falls within the low-z values of up to 12 + log(O/H) = 8.5 to 7.9, and lie in between JWST observations of galaxies with similar redshifts. That underpins the derived trend of O-abundance with z at lower redshifts than those observed by JWST.

10. In addition to physical correlations in this work, there may also be others such as masses of galaxies that could be related to Type II SNe rates, as well as AGN in active or dormant phases. Whereas the role of massive stars in rapid nucleosynthesis of α elements is evident, it would also be of interest to carry out similar spectral studies of other elements such as nitrogen whose abundance proportion to oxygen might indicate possible contributions from slower nucleosynthesis in low-mass AGB stars.

11. Statistical Validation and Uncertainty Quantification: The machine learning component served a dual purpose: (1) providing rapid abundance estimates for future large samples where full photoionization modeling is computationally expensive, and (2) quantifying the predictive power of our physical parameter space. The K-means clustering naturally identified three cosmic epochs with statistically distinct properties ($F = 57.43$, $p < 0.001$). The 95% prediction interval of ±0.246 dex from the Ridge model is comparable to typical measurement uncertainties, suggesting we have captured the dominant physical trends.

6 CONCLUSIONS

The main conclusion of the meta-analysis presented in this paper is that there is a slow but distinct and systematic trend in the decrease of oxygen abundance with increasing redshift up to $z > 10$. The analysis depended on a re-examination of line ratios of [O III] lines, together with [O II] and [S II] calculated line emissivities and observed line intensity ratios. Despite the scatter in derived parameters from a fairly large sample of galaxies, the overall trend and redshift-averaged values appear to lead to the same conclusion. However, the results also demonstrate and confirm earlier observational works based on JWST data that metallicities in high-z galaxies were already significant before a lookback time of up to 13 Gyrs and formation of H II regions by massive stars in the early Universe. While the oxygen abundance is smaller by up to one dex or more compared to galaxies in the present epoch, the deficiency is not larger. In that sense, stellar formation and mass-metallicity relations would appear to hold for high-z galaxies that are similar to evolved ones at low-z, as have been established in previous studies.

We have attempted to expand the analysis beyond what is inferred directly from observational data using a basic machine learning algorithm that validates these trends statistically. The Ridge regression analysis achieves R^2=0.832, confirming the strong Te-abundance anti-correlation. The comprehensive data analytics workflow developed for this study integrates atomic physics calculations, empirical calibrations, and machine learning validation providing a reproducible framework applicable to the larger galaxy samples anticipated from upcoming JWST surveys, enabling systematic constraints on cosmic chemical evolution at scale.

ACKNOWLEDGEMENTS

This work was partially supported by the U.S. National Science Foundation through grant AST-2407470. The R-matrix calculations were carried out at the Ohio Supercomputer Center and on OSU computer clusters. This work applied the following PYTHON package: Astropy(Astropy Collaboration et al. 2013, Astropy Collaboration et al. 2018, and Astropy Collaboration et al. 2022), SciPy(Virtanen et al. 2020), Matplotlib(Hunter 2007), and NumPy(Harris et al. 2020).

DATA AVAILABILITY

The data employed in our studies, including atomic data and line emissivities, are available from the authors.

REFERENCES

Abdurro'uf et al., 2024, JWST NIRSpec High-resolution Spectroscopy of MACS0647-JD at z=10.167: Resolved [OII] Doublet and Electron Density in an Early Galaxy (arXiv:2404.16201), https://arxiv.org/abs/2404.16201

Acharyya A., et al., 2019, Monthly Notices of the Royal Astronomical Society, 488, 5862–5886

Arellano-Córdova K. Z., et al., 2022, The Astrophysical Journal Letters, 940, L23

Arellano-Córdova K. Z., et al., 2025, The JWST EXCELS survey: direct estimates of C, N, and O abundances in two relatively metal-rich galaxies at $\mathbf{z \simeq 5}$ (arXiv:2412.10557), https://arxiv.org/abs/2412.10557

Astropy Collaboration et al., 2013, A&A, 558, A33

Astropy Collaboration et al., 2018, AJ, 156, 123

Astropy Collaboration et al., 2022, ApJ, 935, 167

Berg D. A., et al., 2022, ApJS, 261, 31

Bhattacharya S., Arnaboldi M., Gerhard O., Kobayashi C., Saha K., 2025, Unveiling galaxy chemical enrichment mechanisms out to z 8 from direct determination of O & Ar abundances from JWST/NIRSPEC spectroscopy (arXiv:2408.13396), https://arxiv.org/abs/2408.13396

Bunker A. J., et al., 2024, Astronomy & Astrophysics, 690, A288

Chen Y., et al., 2024, Robust Nitrogen and Oxygen Abundances of Haro 3 from Optical and Infrared Emission (arXiv:2405.18476), https://arxiv.org/abs/2405.18476

Clarke L., et al., 2023, Ultra-deep Keck/MOSFIRE spectroscopic observations of $z \sim 2$ galaxies: direct oxygen abundances and nebular excitation properties (arXiv:2305.07781), https://arxiv.org/abs/2305.07781

Curti M., et al., 2022, Monthly Notices of the Royal Astronomical Society, 518, 425–438

Curti M., et al., 2025, Astronomy & Astrophysics, 697, A89

Decarli R., et al., 2024, Astronomy & Astrophysics, 689, A219

Gburek T., et al., 2019, The Astrophysical Journal, 887, 168

Harikane Y., et al., 2025, JWST & ALMA Joint Analysis with [OII]$\lambda\lambda$3726,3729, [OIII]λ4363, [OIII]88μm, and [OIII]52μm: Multi-Zone Evolution of Electron Densities at $\mathbf{z \sim 0-14}$ and Its Impact on Metallicity Measurements (arXiv:2505.09186), https://arxiv.org/abs/2505.09186

Harris C. R., et al., 2020, Nature, 585, 357

Hsiao T. Y.-Y., et al., 2024, JWST MIRI detections of Hα and [O III] and direct metallicity measurement of the $z = 10.17$ lensed galaxy MACS0647−JD (arXiv:2404.16200)

Hsiao T. Y.-Y., et al., 2025, First direct carbon abundance measured at $z > 10$ in the lensed galaxy MACS0647−JD (arXiv:2409.04625), https://arxiv.org/abs/2409.04625

Hunter J. D., 2007, Computing in Science & Engineering, 9, 90

Inkenhaag A., et al., 2025, First joint absorption and T_e-based metallicity measured in a GRB host galaxy at $z = 4.28$ using JWST/NIRSpec (arXiv:2506.08114), https://arxiv.org/abs/2506.08114

Isobe Y., Ouchi M., Nakajima K., Harikane Y., Ono Y., Xu Y., Zhang Y., Umeda H., 2023, Redshift Evolution of the Electron Density in the ISM at $z \sim 0-9$ Uncovered with JWST/NIRSpec Spectra and Line-Spread Function Determinations (arXiv:2301.06811), https://arxiv.org/abs/2301.06811

Izotov Y. I., Stasińska G., Meynet G., Guseva N. G., Thuan T. X., 2006, Astronomy & Astrophysics, 448, 955–970

Jain S., et al., 2025, A Uniform Analysis of Gas-phase Metallicity Evolution with 1-3 Gyr Time Sampling over the Past 12 Billion Years (arXiv:2508.18369), https://arxiv.org/abs/2508.18369
Li S., et al., 2025, The Astrophysical Journal Letters, 979, L13
Loaiza-Agudelo M., Overzier R. A., Heckman T. M., 2020, The Astrophysical Journal, 891, 19
Matsuoka Y., et al., 2025, SHELLQs. Bridging the gap: JWST unveils obscured quasars in the most luminous galaxies at z > 6 (arXiv:2505.04825), https://arxiv.org/abs/2505.04825
Mingozzi M., et al., 2022, The Astrophysical Journal, 939, 110
Morishita T., et al., 2025, Metallicity Scatter Originating from Sub-kiloparsec Starbursting Clumps in the Core of a Protocluster at z=7.88 (arXiv:2501.11879), https://arxiv.org/abs/2501.11879
Méndez-Delgado J. E., Esteban C., García-Rojas J., Kreckel K., Peimbert M., 2023, Nature, 618, 249–251
Nakajima K., Ouchi M., Isobe Y., Harikane Y., Zhang Y., Ono Y., Umeda H., Oguri M., 2023, JWST Census for the Mass-Metallicity Star-Formation Relations at z=4-10 with the Self-Consistent Flux Calibration and the Proper Metallicity Calibrators (arXiv:2301.12825), https://arxiv.org/abs/2301.12825
Palay E., Nahar S. N., Pradhan A. K., Eissner W., 2012, Monthly Notices of the Royal Astronomical Society: Letters, 423, L35–L39
Rogers N. S. J., Strom A. L., Rudie G. C., Trainor R. F., Raptis M., von Raesfeld C., 2024, CECILIA: Direct O, N, S, and Ar Abundances in Q2343-D40, a Galaxy at z ~3 (arXiv:2312.08427), https://arxiv.org/abs/2312.08427
Sanders R. L., et al., 2016, The Astrophysical Journal Letters, 825, L23
Sanders R. L., Shapley A. E., Topping M. W., Reddy N. A., Brammer G. B., 2023b, Direct Te-based Metallicities of z=2-9 Galaxies with JWST/NIRSpec: Empirical Metallicity Calibrations Applicable from Reionization to Cosmic Noon (arXiv:2303.08149), https://arxiv.org/abs/2303.08149
Sanders R. L., Shapley A. E., Topping M. W., Reddy N. A., Brammer G. B., 2023a, Excitation and Ionization Properties of Star-forming Galaxies at z=2.0-9.3 with JWST/NIRSpec (arXiv:2301.06696), https://arxiv.org/abs/2301.06696
Sarkar A., et al., 2024, Unveiling the Cosmic Chemistry: Revisiting the Mass-Metallicity Relation with JWST/NIRSpec at 4 < z < 10 (arXiv:2408.07974), https://arxiv.org/abs/2408.07974
Stiavelli M., et al., 2024, What can we learn from the Nitrogen abundance of High-z galaxies? (arXiv:2412.06517), https://arxiv.org/abs/2412.06517
Storey P. J., Sochi T., 2015, Monthly Notices of the Royal Astronomical Society, 449, 2974–2979
Virtanen P., et al., 2020, Nature Methods, 17, 261
Welch B., et al., 2024, TEMPLATES: Direct Abundance Constraints for Two Lensed Lyman-Break Galaxies (arXiv:2401.13046), https://arxiv.org/abs/2401.13046
Welch B., et al., 2025, The Sunburst Arc with JWST: III. An Abundance of Direct Chemical Abundances (arXiv:2405.06631), https://arxiv.org/abs/2405.06631
Witstok J., et al., 2024, Monthly Notices of the Royal Astronomical Society, 536, 27–50
Zhang Y., Morishita T., Stiavelli M., 2025, Potential Nitrogen Enrichment via Direct-Collapse Wolf-Rayet Stars in a z = 4.7 Star-Forming Galaxy (arXiv:2502.04817), https://arxiv.org/abs/2502.04817
Zhu C., et al., 2025, The Physical Origin of Extreme Emission Line Galaxies at High redshifts: Strong [OIII] Emission Lines Produced by Obscured AGNs (arXiv:2410.12198), https://arxiv.org/abs/2410.12198

APPENDIX A: DATA COLLECTION OF ANALYSIS RESULTS AND LINE FLUXES FROM LITERATURE

Table A1. A holistic table of line fluxes from other papers. All line fluxes are normalized by Hβ = 1.

Galaxy	z	OII3726	OII3729	OIII4363	OIII4959	OIII5007	SII6718	SII6732	OII7320	OII7330	Hβ Flux ($erg\ s^{-1}\ cm^{-2}$)
Haro3	0.003208	1.243	1.577	0.02521	1.361	4.016	0.1461	0.1172	-	-	-
J0021+0052	0.09839	0.6407	0.7217	0.02202	1.537[c]	4.427	0.1819	0.1312	0.02554	0.01982	$2.271 \cdot 10^{-14}$
J032845.99+011150.8	0.142181	2.154[a]	-	0.01280	0.7333	2.294	0.2849	0.2191	0.02312	0.01920	$2.812 \cdot 10^{-15}$
J015028.39+130858.4	0.146712	2.220[a]	-	0.01650	0.7424	2.221	0.2570	0.2205	0.01881	0.01568	$6.059 \cdot 10^{-15}$
J124509.05+104340.1	0.165569	1.775[a]	-	0.02845	1.718	5.122	0.1714	0.1435	0.02856	0.02243	$8.648 \cdot 10^{-15}$
J005527.45–002148.7	0.167449	2.008[a]	-	0.02228	1.236	3.673	0.1768	0.1573	0.03513	0.02718	$1.611 \cdot 10^{-14}$
J101629.88+073404.9	0.18271	2.271[a]	-	0.05832	1.729	5.236	0.1475	0.1231	0.02264	0.01852	$7.288 \cdot 10^{-15}$
J082247.66+224144.0	0.216226	2.090[a]	-	0.06771	1.924	5.814	0.1329	0.1225	0.03747	0.02757	$8.994 \cdot 10^{-15}$
J084034.10+134451.3	0.226961	1.785[a]	-	0.04537	1.784	5.353	0.1842	0.1465	0.02768	0.02191	$2.601 \cdot 10^{-15}$
GOODS-N-14595	1.67596	0.5759	0.6161	0.08929	1.692	4.960	0.2500	<0.5446	-	-	$2.240 \cdot 10^{-17}$
GOODS-N-8240	1.6909	0.5944	0.6285	0.04954	1.458	4.434	<0.9659	<5.399	-	-	$3.230 \cdot 10^{-17}$
RCSGA032727-132609	1.7	1.133	0.9876	0.05637	1.543	4.900	0.1448	0.1066	-	-	$4.495 \cdot 10^{-15}$
SGAS1723+34	1.3293	-	-	0.07480	2.084	6.239	0.1447	0.1076	0.02103	0.01935	$1.845 \cdot 10^{-15}$
NIRSpec3753	1.768	2.692[a]	-	0.1169	1.270	4.040	0.2770	0.2361	-	-	$8.810 \cdot 10^{-18}$
CEERS-3506	2.055	-	-	0.2350	2.530	6.510	0.01360	0.02230	0.007100	0.004200	$2.210 \cdot 10^{-17}$
CEERS-3788	2.295	0.4170	0.4590	0.08800	2.370	7.010	0.3720	0.2330	-	-	-
Sunburst Arc	2.37	0.2900	0.2200	0.1380	2.200	6.800	0.03900	0.04300	0.03000	0.02200	$6.600 \cdot 10^{-19}$
A1689-217	2.5918	1.156	1.339	0.1094	2.156	6.210[c]	-	-	-	-	$1.920 \cdot 10^{-16}$
SGAS1226+21	2.925	-	-	<0.04707	1.320	4.327	0.3045	0.2917	<0.006973	<0.006973	$1.721 \cdot 10^{-16}$
Q2343-D40	2.963	-	-	0.08700	1.993	5.914	0.1310	0.09700	0.02500	0.02000	$8.650 \cdot 10^{-18}$
Q2343-D40	2.963	-	-	0.04000	2.254	7.075	0.1310	0.09700	0.02500	0.02000	-
COSMOS-1908	3.08	0.2309	0.2309	0.1186	2.288	7.055	-	-	-	-	$4.720 \cdot 10^{-17}$
CEERS-11088	3.302	1.681[a]	-	0.05737	2.041	6.052	0.2147	0.1714	0.07257[b]	-	$2.632 \cdot 10^{-17}$
CEERS-11088	3.302	0.5200	0.4700	0.08800	1.936	6.233	0.5830	0.2570	-	-	-
JADES-19519	3.604	0.3790	0.5330	0.2010	2.279	6.782	-	-	-	-	-
GLASS-160133	4.015	0.2140	0.2610	0.1540	2.559	7.725	-	-	-	-	-
GTO1199-150880	4.247	1.006[a]	-	0.1358	10.26[d]	-	0.08447	0.06849	-	-	$8.760 \cdot 10^{-18}$
GRB050505	4.28	0.7037	0.9722	0.1389	2.065	6.046	0.2778	0.2037	-	-	$1.080 \cdot 10^{-17}$
CEERS-1665	4.482	1.514[a]	-	0.06532	2.214	6.827	0.1512	0.1243	<0.08772[b]	-	$2.679 \cdot 10^{-17}$
CEERS-1665	4.488	0.5120	0.3520	0.06700	2.338	7.336	0.3100	0.2030	-	-	-
CEERS-1746	4.56	1.120[a]	-	0.1624	2.251	7.604	0.09117	0.09687	<0.1425[b]	-	$3.510 \cdot 10^{-18}$
GLASS-150029	4.584	0.1780	0.2070	0.1840	2.328	6.588	-	-	-	-	-
GLASS-150029	4.584	0.1827	0.2373	0.1530	2.221	6.316	-	-	-	-	-
ID60001	4.6928	0.5650[a]	-	0.1640	2.170	6.470	0.04374	0.03645	-	-	$8.230 \cdot 10^{-18}$
EXCELS-121806	5.225	0.8411[a]	-	0.1339	2.327	6.826	0.05920	0.04835	-	-	$4.054 \cdot 10^{-18}$
EXCELS-70864	5.255	0.8541[a]	-	0.1108	2.854	8.617	<0.03900	<0.04446	-	-	$2.564 \cdot 10^{-18}$
J1211-0118	6.031	0.9760	1.163	<0.06200	1.605	4.783	-	-	-	-	$1.260 \cdot 10^{-17}$
J0217-0208	6.204	0.8930	0.6030	0.07500	2.004	6.567	-	-	-	-	$1.880 \cdot 10^{-17}$
J0217-0208	6.204	0.8930	0.6030	0.09592	2.234[c]	6.433	0.08931	0.09482	-	-	$9.070 \cdot 10^{-18}$
PJ308-21	6.2342	0.5/1.0/2.0[ac]	-	0.1139	2.293	6.873	0.1418	0.1721	-	-	$1.650 \cdot 10^{-17}$
SXDF-NB1006-2	7.212	0.2660	0.2390	0.1130	2.262	6.741	-	-	-	-	$8.550 \cdot 10^{-18}$
GLASS-10021	7.286	0.3378	0.4730	0.1980	2.696	8.284	-	-	-	-	$7.400 \cdot 10^{-18}$
ERO6355	7.6651	0.5104	0.3896	0.1000	2.660	8.290	-	-	-	-	$2.110 \cdot 10^{-18}$
ZD12	7.8762	0.3300	0.2791	0.2529	7.051[d]	-	-	-	-	-	$6.090 \cdot 10^{-19}$
JADES-GS-z8-0-LA	8.48523	0.1402	0.08785	0.1776	1.836	5.470	-	-	-	-	$3.210 \cdot 10^{-19}$
CEERS-1019	8.6791	0.2084	0.1781	0.1780	2.262	7.011	-	-	-	-	$1.017 \cdot 10^{-17}$
JADES-GS-z8-1-LA	8.71523	0.2667	0.2309	0.2010	2.401	7.153	-	-	-	-	$8.360 \cdot 10^{-19}$
JADES-GS-z9-0	9.4327	0.07825	0.07294	0.1790	1.756	4.955	-	-	-	-	$7.540 \cdot 10^{-19}$
MACS0647-JD1	10.167	0.1038	0.07022	0.1130	2.396[c]	6.900	-	-	-	-	$3.275 \cdot 10^{-18}$

[a] This is the blended flux for OII3726+OII3729.
[b] This is the blended flux for OII7320+OII7330.
[c] This is not come from papers, it is come from assumptions as shown in the text of Appendix A
[d] This is the blended flux for OIII4959+OIII5007.

Table A1. Line flux data sources of galaxies

Source	Instrument	Adopted line flux data of galaxies
Acharyya et al. (2019)	Keck/NIRSPEC	All data of RCSGA032727-132609.
Chen et al. (2024)	Keck/KCWI	All data of Haro3.
Clarke et al. (2023)	Keck/MOSFIRE	All data of GOODS-N-14595 and GOODS-N-8240.
Loaiza-Agudelo et al. (2020)	VLT/XShooter	All data of J032845.99+011150.8, J015028.39+130858.4, J124509.05+104340.1, J005527.45–002148.7, J101629.88+073404.9, J082247.66+224144.0,and J084034.10+134451.3.
Mingozzi et al. (2022)	CLASSY	All data of J0021+0052.
Sanders et al. (2016)	MOSDEF	All data of COSMOS-1908.
Arellano-Córdova et al. (2025)	JWST/NIRSpec	All data of EXCELS-121806 and EXCELS-70864.
Bhattacharya et al. (2025)	JWST/NIRSpec	All data of CEERS-3788, the second row of CEERS-11088, the first row of GLASS-150029, JADES-19519, and the second row of CEERS-1665. OIII4363, OIII4960, and OIII5008 line fluxes of the second row of Q2343-D40.
Decarli et al. (2024)	JWST/NIRSpec	All data of PJ308-21.
Harikane et al. (2025)	JWST/NIRSpec	All data of J1211-0118, SXDF-NB1006-2, and first row of J0217-0208. Line fluxes of OII 3726 and 3729 lines of the second row of J0217-0208
Sanders et al. (2023b)	JWST/NIRSpec	Blended line flux of OII 3726 and 3729 lines and all other line flux data of CEERS-1019. All data of CEERS-1746, the first row of CEERS-11088, and the first row of CEERS-1665.
Isobe et al. (2023)	JWST/NIRSpec	OII 3726 and 3729 lines ratio of CEER-1019, ERO6355, GLASS-160133, and the second row of GLASS-150029.
Curti et al. (2022)	JWST/NIRSpec	Blended flux of OII 3726 and 3729 lines and all other line flux data of ERO6355.
Hsiao et al. (2025)	JWST/NIRSpec	Line flux OIII 5007(=226 $\cdot$ 10^{-19} $erg\ s^{-1}\ cm^{-2}$) of MACS0647-JD1.
Hsiao et al. (2024)	JWST/NIRSpec	OIII5007/Hbeta(=6.9) ratio of MACS0647-JD1.
Abdurro'uf et al. (2024)	JWST/NIRSpec	OII3726, OII3729, and OIII4363 line fluxes of MACS0647-JD1.
Welch et al. (2024)	JWST/NIRSpec	All data of SGAS1226+21 and SGAS1723+34.
Welch et al. (2025)	JWST/NIRSpec	All data of Sunburst Arc.
Matsuoka et al. (2025)	JWST/NIRSpec	All data except for fluxes of OII 3726 and 3729 lines of the second row of J0217-0208.
Rogers et al. (2024)	JWST/NIRSpec	All data of the first row of Q2343-D40. SII6718, SII6732, OII7320, and OII7330 line fluxes of the second row of Q2343-D40.
Nakajima et al. (2023)	JWST/NIRSpec	Blended line flux of OII 3726 and 3729 lines and all other line flux data of the second row of GLASS-150029, GLASS-10021, and GLASS-160133.
Curti et al. (2025)	JWST/NIRSpec	All data of JADES-GS-z9-0.
Witstok et al. (2024)	JWST/NIRSpec	All data of JADES-GS-z8-1-LA and JADES-GS-z8-0-LA.
Zhu et al. (2025)	JWST/NIRSpec	All data of CEERS-3506
Gburek et al. (2019)	Keck/MOSFIRE	All data of A1689-217.
Bunker et al. (2024)	JWST/NIRSpec	All data of NIRSpec3753.
Inkenhaag et al. (2025)	JWST/NIRSpec	All data of GRB050505.
Li et al. (2025)	JWST/NIRSpec	OII 3726 and 3729 lines ratio of GLASS-10021.
Morishita et al. (2025)	JWST/NIRSpec	All data of ZD12.
Stiavelli et al. (2024)	JWST/NIRSpec	All data of GTO1199-150880.
Zhang et al. (2025)	JWST/NIRSpec	All data of ID60001.

Table A2. A holistic table of analysis results by using Storey & Sochi (2015) EIE data

Galaxy	Instrument	z	$12+\log(O/H)$ Izotov Formula	$12+\log(O/H)$ MD Formula[d]	$12+\log(O/H)$ Original Papar	$T_e[OIII]$ (K)	$N_e[OII]$ (cm^{-3})	$N_e[SII]$ (cm^{-3})
Haro3	Keck/KCWI	0.003208	8.44	8.38	8.309	9900	145	183
J0021+0052	CLASSY	0.09839	8.44	8.43	8.17[e]	9400	275	50
J032845.99+011150.8	VLT/XShooter	0.142181	8.30	8.41	8.30	9600	-	126
J015028.39+130858.4	VLT/XShooter	0.146712	8.17	8.33	8.30	10400	-	283
J124509.05+104340.1	VLT/XShooter	0.165569	8.48	8.41	8.54	9600	-	245
J005527.45–002148.7	VLT/XShooter	0.167449	8.37	8.39	8.47	9800	-	343
J101629.88+073404.9	VLT/XShooter	0.18271	8.18	8.16	8.33	12000	-	239
J082247.66+224144.0	VLT/XShooter	0.216226	8.19	8.15	8.39	12100	-	412
J084034.10+134451.3	VLT/XShooter	0.226961	8.30	8.27	8.37	10900	-	170
SGAS1723+34	JWST/NIRSpec	1.3293	8.17	8.12	8.13	12300	-	80
GOODS-N-14595	Keck/MOSFIRE	1.67596	7.86	7.89	>7.62	14500	391	-
GOODS-N-8240	Keck/MOSFIRE	1.6909	8.04	8.15	8.02	12100	377	-
RCSGA032727-132609	Keck/NIRSPEC	1.7	8.14/8.13[a]	8.15	8.19	12100	726	68
NIRSpec3753	JWST/NIRSpec	1.768	7.63	7.49	-	18200	-	275
CEERS-3506	JWST/NIRSpec	2.055	7.56	7.23	7.52	20700	-	3755
CEERS-3788	JWST/NIRSpec	2.295	8.16	8.11	7.91	12400	320	-
Sunburst Arc	JWST/NIRSpec	2.37	7.89	7.82	7.97	15100	1196	870
A1689-217	Keck/MOSFIRE	2.5918	7.87	7.69	8.06	16400	284	-
SGAS1226+21	JWST/NIRSpec	2.925	>7.94	>8.17	>8.04	<11900	-	489
Q2343-D40	JWST/NIRSpec	2.963	8.05	8.02	8.07	13300	-	73
Q2343-D40	JWST/NIRSpec	2.963	8.63	8.41	8.01[f]	9600	-	80
COSMOS-1908	MOSDEF	3.08	7.99	7.94	8.00	14000	491	-
CEERS-11088	JWST/NIRSpec	3.302	8.27	8.22	8.33	11400	-	175
CEERS-11088	JWST/NIRSpec	3.302	8.05	8.04	7.87[f]	13100	668	-
JADES-19519	JWST/NIRSpec	3.604	7.70	7.46	7.48	18500	58	-
GLASS-160133	JWST/NIRSpec	4.015	8.01	7.92	7.95[g]	14200	204	-
GTO1199-150880	JWST/NIRSpec	4.247	8.02	7.90	8.00	14400	-	195
GRB050505	JWST/NIRSpec	4.28	7.84	7.72	7.80	16100	73	53
CEERS-1665	JWST/NIRSpec	4.482	8.29	8.22	8.27	11400	-	217
CEERS-1665	JWST/NIRSpec	4.488	8.32	8.24	8.13	11200	1405	-
CEERS-1746	JWST/NIRSpec	4.56	7.92	7.77	7.95	15600	-	766
GLASS-150029	JWST/NIRSpec	4.584	7.71	7.54	7.53	17800	294	-
GLASS-150029	JWST/NIRSpec	4.584	7.76	7.66	7.70[g]	16600	143	-
ID60001	JWST/NIRSpec	4.6928	7.75	7.62	7.75	17000	-	236
EXCELS-121806	JWST/NIRSpec	5.225	7.94	7.85	7.97	14900	-	205
EXCELS-70864	JWST/NIRSpec	5.255	8.23	8.10	8.21	12500	-	~961[c]
J1211-0118	JWST/NIRSpec	6.031	>8.08	>8.09	8.51	<12600	226	-
J0217-0208	JWST/NIRSpec	6.204	8.22	8.16	8.20	12000	1526	-
J0217-0208	JWST/NIRSpec	6.204	8.07	8.01	-	13400	-	743
PJ308-21	JWST/NIRSpec	6.2342	7.99/8.02/8.07[b]	7.95	-	13900	-	1206
SXDF-NB1006-2	JWST/NIRSpec	7.212	7.98	7.94	7.99	14000	701	-
GLASS-10021	JWST/NIRSpec	7.286	7.88	7.67	7.87[g]	16500	61	-
ERO6355	JWST/NIRSpec	7.6651	8.24	8.12	8.24[h]	12300	1074	-
ZD12	JWST/NIRSpec	7.8762	7.30	6.71	7.34	25500	1007	-
JADES-GS-z8-0-LA	JWST/NIRSpec	8.48523	7.54	7.37	7.481	19300	2329	-
CEERS-1019	JWST/NIRSpec	8.6791	7.77	7.62	7.78[i]	17000	893	-
JADES-GS-z8-1-LA	JWST/NIRSpec	8.71523	7.72	7.52	7.699	17900	885	-
JADES-GS-z9-0	JWST/NIRSpec	9.4327	7.32	7.21	7.41	20800	743	-
MACS0647-JD1	JWST/NIRSpec	10.167	7.98	7.95	7.79[j]	13900	1613	-

[a] Left value is calculated by using $N_e[OII]$, and the right is by using $N_e[SII]$. Other galaxies with using both OII and SII electron density give same electron temperature and oxygen abundance, so they are just listed as one electron temperature and oxygen abundance value.

[b] From 3 assumptions of OII3726+OII3729 flux 0.5/1.0/2.0 respectively

[c] Upper limit of both SII lines are used to get the line ratio, so it is a uncertain value.

[d] Méndez-Delgado Formula. The uncertainty of $12+\log(O/H)$ derived by this formula for all galaxies is about 0.2.

[e] (Berg et al. 2022)

[f] (Bhattacharya et al. 2025)

[g] (Nakajima et al. 2023)

[h] (Curti et al. 2022)

[i] (Sanders et al. 2023b)

[j] (Hsiao et al. 2024)